

<sup>1</sup> **Cross-scale interaction of host tree size and climatic water deficit**  
<sup>2</sup> **governs bark beetle-induced tree mortality**

<sup>3</sup> Michael J. Koontz<sup>1,2,3\*</sup>, Andrew M. Latimer<sup>1,2</sup>, Leif A. Mortenson<sup>4</sup>, Christopher J. Fettig<sup>5</sup>, Malcolm P.  
<sup>4</sup> North<sup>1,2,6</sup>

<sup>5</sup> <sup>1</sup>Graduate Group in Ecology, University of California, Davis, CA, USA

<sup>6</sup> <sup>2</sup>Department of Plant Sciences, University of California, Davis, CA, USA

<sup>7</sup> <sup>3</sup>Earth Lab, University of Colorado-Boulder; Boulder, CO, USA

<sup>8</sup> <sup>4</sup>USDA Forest Service, Pacific Southwest Research Station, Placerville, CA, USA

<sup>9</sup> <sup>5</sup>USDA Forest Service, Pacific Southwest Research Station, Davis, CA, USA

<sup>10</sup> <sup>6</sup>USDA Forest Service, Pacific Southwest Research Station, Mammoth Lakes, CA, USA

<sup>11</sup> \*Correspondence: michael.koontz@colorado.edu

<sup>12</sup> *Keywords:* *Dendroctonus brevicomis*, disturbance, drones, *Pinus ponderosa*, Sierra Nevada, structure from motion, forest structure, climate change-type drought, macroecology

<sup>14</sup> *Abstract word count:* 310

<sup>15</sup> *Overall .docx word count:* 11499

<sup>16</sup> *Main text word count:* 4034 (Intro: 1264 Results: 368 (41+110+217); Discussion: 2402)

<sup>17</sup> *Methods word count:* 3093 (661+642+1463+327)

<sup>18</sup> *Text boxes word count:* 0

<sup>19</sup> Date report generated: April 14, 2020

<sup>20</sup> **Abstract**

<sup>21</sup> The Californian hot drought of 2012 to 2015 created favorable conditions for unprecedented ponderosa pine  
<sup>22</sup> (*Pinus ponderosa*) mortality in the Sierra Nevada mountain range, largely attributable to the western pine  
<sup>23</sup> beetle (*Dendroctonus brevicomis*; WPB). Climate conditions and forest density may interact to affect tree  
<sup>24</sup> mortality, but density is a coarse gauge of forest structure that can affect WPB behavior in a number of  
<sup>25</sup> ways. Measuring broad-scale climate conditions simultaneously with local forest composition and structure–  
<sup>26</sup> the spatial distribution and size of trees– will refine our understanding of how these variables interact, but is  
<sup>27</sup> generally expensive and/or labor-intensive. We use drone surveys over a network of 160 field plots along a 350-  
<sup>28</sup> km latitudinal and 1000-m elevational gradient in western slope Sierra Nevada ponderosa pine/mixed-conifer  
<sup>29</sup> forests and structure from motion (SfM) processing to segment and classify more than 450,000 trees over 9

30 km<sup>2</sup> of forest with WPB-induced tree mortality. We modeled the probability of ponderosa pine mortality as a  
31 function of forest structure and composition and their interaction with site-level climatic water deficit (CWD),  
32 accounting for spatial covariance using exact Gaussian processes. A greater local proportion of host trees  
33 strongly increased the probability of host mortality, with greater host density amplifying this effect. Further,  
34 we found a strong interaction between host size and CWD such that larger trees increased the probability of  
35 host mortality at hot/dry sites, but smaller trees tended to drive mortality in cool/wet sites.  
36 Our results demonstrate a variable response of WPB to local forest structure and composition across an  
37 environmental gradient, which may help reconcile differences between observed ecosystem-wide tree mortality  
38 patterns and predictions from models based on coarser-scale forest structure. Climate change adaptation  
39 strategies should consider that future disturbance outcomes may depend on interactions between local forest  
40 structure and broad-scale environmental gradients, with the potential for cross-scale interactions that challenge  
41 our current understanding of forest insect dynamics.

## 42 Introduction

43 Bark beetles dealt the final blow to many of the nearly 150 million trees killed in the California hot drought  
44 of 2012 to 2015 and its aftermath (USDAFS 2019). A harbinger of climate change effects to come, record  
45 high temperatures exacerbated the drought (Griffin and Anchukaitis 2014), which increased water stress in  
46 trees (Asner et al. 2016), making them more susceptible to colonization by bark beetles (Fettig 2012, Kolb  
47 et al. 2016). Further, a century of fire suppression policy has enabled forests to grow into dense stands,  
48 which can also makes them more vulnerable to bark beetles (Fettig 2012). This combination of environmental  
49 conditions and forest structural characteristics led to tree mortality events of unprecedented size in the  
50 driest, densest forests across the state (Young et al. 2017). The mechanisms underlying the link between  
51 tree susceptibility to colonization by insects and hot, dry conditions are often directly attributed to tree  
52 physiology (Bentz et al. 2010, Kolb et al. 2016), while the link to forest density is multifaceted (Fettig 2012).  
53 Because forest density is a coarse metric of the forest features to which bark beetles respond (Raffa et al.  
54 2008), our understanding of the connection between forest density and insect disturbance severity could  
55 be enhanced with more finely-resolved measures of forest structure as well as explicit consideration of tree  
56 species composition (Stephenson et al. 2019, Fettig et al. 2019). Finally, the challenge of simultaneously  
57 measuring the effects of both local-scale forest features (such as structure and composition) and broad-scale  
58 environmental conditions (such as climatic water deicit; CWD) on forest insect disturbance leaves their  
59 interaction effect relatively underexplored (Seidl et al. 2016, Stephenson et al. 2019, Fettig et al. 2019).  
60 The ponderosa pine/mixed-conifer forests in California's Sierra Nevada region are characterized by regular

61 bark beetle disturbances, primarily by the influence of western pine beetle (*Dendroctonus brevicomis*; WPB)  
62 on its host ponderosa pine (*Pinus ponderosa*) (Fettig 2016). WPB is a primary bark beetle— its reproductive  
63 success is contingent upon host tree mortality, which itself requires enough beetles to mass attack the host tree  
64 and overwhelm its defenses (Raffa and Berryman 1983). This Allee effect creates a strong coupling between  
65 beetle selection behavior of host trees and host tree susceptibility to colonization (Raffa and Berryman  
66 1983, Logan et al. 1998). A key defense mechanism of conifers to bark beetle attack is to flood beetle bore  
67 holes with resin, which physically expels beetles and may interrupt beetle communication (Franceschi et al.  
68 2005, Raffa et al. 2015). Under normal conditions, weakened trees with compromised defenses are the most  
69 susceptible to colonization and will be the main targets of primary bark beetles like WPB (Bentz et al. 2010,  
70 Raffa et al. 2015). Under severe water stress, many trees no longer have the resources available to mount  
71 a defense (Kolb et al. 2016) and thus prolonged drought can often trigger increased bark beetle-induced  
72 tree mortality as average tree vigor declines (Bentz et al. 2010). As the local population density of beetles  
73 increases due to successful reproduction within spatially-aggregated weakened trees, as might occur during  
74 drought, mass attacks grow in size and become capable of overwhelming formidable tree defenses such that  
75 even healthy trees may be susceptible to colonization and mortality (Bentz et al. 2010, Raffa et al. 2015).  
76 Thus, water stress can be a key determinant of whether individual trees are susceptible to bark beetles under  
77 many conditions, and this environmental condition may interact with beetle population dynamics to drive  
78 tree susceptibility under extreme conditions (Bentz et al. 2010, Stephenson et al. 2019).

79 WPB activity is strongly influenced by forest structure— the spatial distribution and size of trees— and tree  
80 species composition. Taking forest structure alone, high-density forests are more prone to bark beetle-induced  
81 tree mortality (Fettig 2012) which may arise as greater competition for water resources amongst crowded trees  
82 and thus average tree resistance is lower (Hayes et al. 2009), or because smaller gaps between trees protect  
83 pheromone plumes from dissipation by the wind and thus enhance intraspecific beetle communication (Thistle  
84 et al. 2004). Tree size is another aspect of forest structure that affects bark beetle host selection behavior  
85 with smaller trees tending to have lower capacity for resisting attack, and larger trees being more desirable  
86 targets on account of their thicker phloem providing greater nutritional content (Chubaty et al. 2009, Graf et  
87 al. 2012). Taking forest composition alone, WPB activity in the Sierra Nevada mountain range of California  
88 is necessarily tied to the regional distribution of its exclusive host, ponderosa pine (Fettig 2016). Colonization  
89 by primary bark beetles can also depend on the relative frequencies of tree species in a more local area, akin  
90 to reduced oligophagous insect herbivory in forests comprising taxonomically-distinct tree species compared  
91 to monocultures (Jactel and Brockerhoff 2007). The interaction between forest structure and composition  
92 also drives WPB activity. For instance, high-density forests with high host availability may experience greater

93 beetle-induced tree mortality because dispersal distances between potential host trees are shorter reducing  
94 predation of adults searching for hosts and facilitating higher rates of colonization (Miller and Keen 1960,  
95 Berryman 1982, Fettig et al. 2007) or because high host availability reduces the chance of individual beetles  
96 wasting their limited resources flying to and landing on a non-host tree (Moeck et al. 1981, Evenden et  
97 al. 2014). Stand-scale measures of forest structure and composition thus paint a fundamentally limited  
98 picture of the mechanisms by which these forest characteristics affect bark beetle disturbance, but finer-grain  
99 information explicitly recognizing tree size, tree species, and local tree density should more appropriately  
100 capture the ecological processes underlying insect-induced tree mortality. Additionally, considering the  
101 effects of local forest structure and composition with the effects of environmental conditions may help refine  
102 our understanding of tree mortality patterns in widespread events such as during the recent California hot  
103 drought.

104 The vast spatial extent of tree mortality in the 2012 to 2015 California hot drought challenges our ability to  
105 simultaneously consider how broad-scale environmental conditions may interact with local forest structure  
106 and composition to affect the dynamic between bark beetle selection and colonization of host trees, and host  
107 tree susceptibility to attack (Anderegg et al. 2015, Stephenson et al. 2019). Measuring local forest structure  
108 generally requires expensive instrumentation (Kane et al. 2014, Asner et al. 2016) or labor-intensive field  
109 surveys (Larson and Churchill 2012, Stephenson et al. 2019, Fettig et al. 2019), which constrains survey  
110 extent and frequency. Small, unhumanned aerial systems (sUAS) enable relatively fast and cheap remote  
111 imaging over dozens of hectares of forest, which can be used to measure complex forest structure at the  
112 individual tree scale (Morris et al. 2017, Shiklomanov et al. 2019). Distributing such surveys across an  
113 environmental gradient can overcome the data acquisition challenge inherent in investigating phenomena  
114 with both a strong local- and a strong broad-scale component.

115 We used ultra-high resolution, sUAS-derived remote sensing data over a network of 32 sites in Sierra Nevada  
116 ponderosa pine/mixed-conifer forests spanning 1000 m of elevation and 350 km of latitude (see Fettig et  
117 al. 2019) and covering a total of 9 km<sup>2</sup> to ask how broad-scale environmental conditions interacted with  
118 local forest structure and composition to affect the probability of tree mortality during the cumulative tree  
119 mortality event of 2012 to 2018. We asked:

- 120 1. How does the proportion of host trees in a local area and average host tree size affect WPB-induced  
121 tree mortality?
- 122 2. How does the density of all tree species (hereafter “overall density”) affect WPB-induced tree mortality?
- 123 3. How does environmentally-driven tree moisture stress affect WPB-induced tree mortality?

124        4. Do the effects of forest structure, forest composition, and environmental condition interact to influence  
125           WPB-induced tree mortality?

126        **Methods**

127        **Study system**

128        We built our study coincident with 160 vegetation/forest insect monitoring plots at 32 sites established  
129        between 2016 and 2017 by Fettig et al. (2019) (Figure 1). The study sites were chosen to reflect typical  
130        west-side Sierra Nevada yellow pine/mixed-conifer forests and were dominated by ponderosa pine (Fettig  
131        et al. 2019). Plots were located in WPB-attacked, yellow pine/mixed-conifer forests across the Eldorado,  
132        Stanislaus, Sierra and Sequoia National Forests and were stratified by elevation (914-1219 m, 1219-1524  
133        m, 1524-1829 m above sea level). In the Sequoia National Forest, the southernmost National Forest in our  
134        study, plots were stratified with the lowest elevation band of 1219-1524 m and extended to an upper elevation  
135        band of 1829-2134 m to capture a more similar forest community composition as at the more northern  
136        National Forests. The sites have variable forest structure and plot locations were selected in areas with >35%  
137        ponderosa pine basal area and >10% ponderosa pine mortality. At each site, five 0.041 ha circular plots  
138        were installed along transects with 80 to 200m between plots. In the field, Fettig et al. (2019) mapped all  
139        stem locations relative to the center of each plot using azimuth/distance measurements. Tree identity to  
140        species, tree height, and diameter at breast height (DBH) were recorded if DBH was greater than 6.35cm.  
141        Year of mortality was estimated based on needle color and retention if it occurred prior to plot establishment,  
142        and was directly observed thereafter during annual site visits. A small section of bark (approximately 625  
143        cm<sup>2</sup>) on both north and south aspects was removed from dead trees to determine if bark beetle galleries  
144        were present. The shape, distribution, and orientation of galleries are commonly used to distinguish among  
145        bark beetle species (Fettig 2016). In some cases, deceased bark beetles were present beneath the bark to  
146        supplement identifications based on gallery formation. During the spring and early summer of 2018, all field  
147        plots were revisited to assess whether dead trees had fallen (Fettig et al. 2019).

148        In the typical life cycle of WPBs, females initiate host colonization by tunneling through the outer bark and  
149        into the phloem and outer xylem where they rupture resin canals.

150        As a result, oleoresin exudes and collects on the bark surface, as is commonly observed with other bark beetle  
151        species. During the early stages of attack, females release an aggregation pheromone component which, in  
152        combination with host monoterpenes released from pitch tubes, is attractive to conspecifics (Bedard et al.  
153        1969). An antiaggregation pheromone component is produced during latter stages of host colonization by  
154        several pathways, and is thought to reduce intraspecific competition by altering adult behavior to minimize

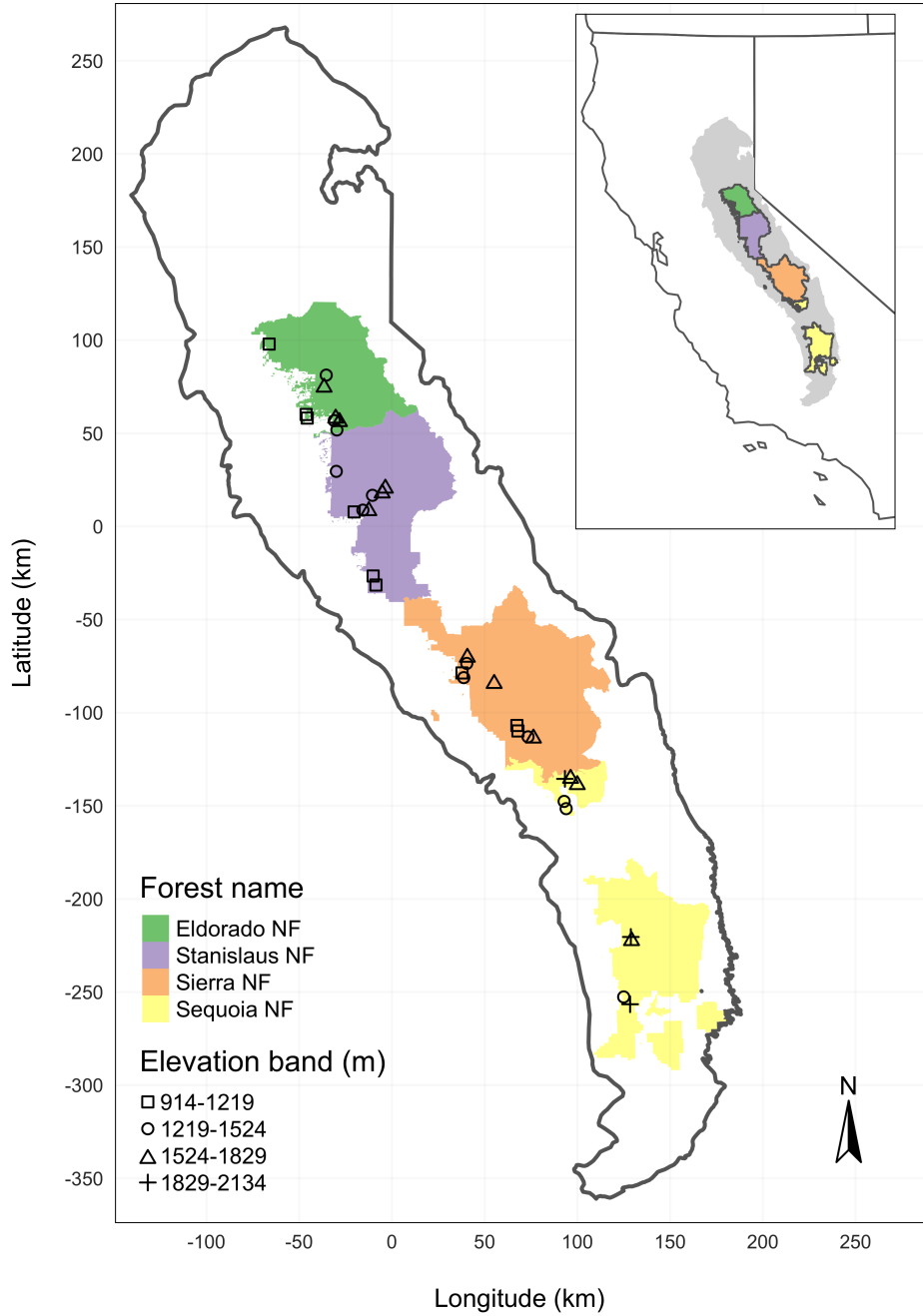


Figure 1: The network of field plots spanned a 350-km latitudinal gradient from the Eldorado National Forest in the north to the Sequoia National Forest in the south. Plots were stratified by three elevation bands in each forest, with the plots in the Sequoia National Forest (the southern-most National Forest) occupying elevation bands 305 m above the three bands in the other National Forests in order to capture a similar community composition.

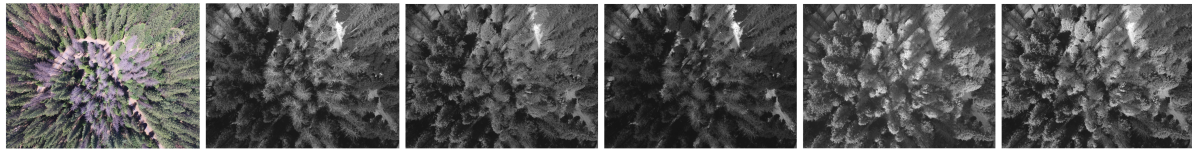
155 overcrowding of developing brood within the host (Byers and Wood 1980). Volatiles from several nonhosts  
156 sympatric with ponderosa pine have been demonstrated to inhibit attraction of WPB (Shepherd et al. 2007,  
157 Fettig and Hilszczański 2015). In California, WPB generally has 2-3 generations in a single year and can  
158 often out-compete its congener, the mountain pine beetle, *Dendroctonus ponderosae*, in ponderosa pines,  
159 especially in larger trees (Miller and Keen 1960).

160 **Aerial data collection and processing**

161 Nadir-facing imagery was captured using a gimbal-stabilized DJI Zenmuse X3 broad-band red/green/blue  
162 (RGB) camera (DJI 2015a) and a fixed-mounted Micasense Rededge3 multispectral camera with five narrow  
163 bands (Micasense 2015) on a DJI Matrice 100 aircraft (DJI 2015b). Imagery was captured from both cameras  
164 along preprogrammed aerial transects over ~40 hectares surrounding each of the 32 sites (each of these  
165 containing five field plots) and was processed in a series of steps to yield local forest structure and composition  
166 data suitable for our statistical analyses. All images were captured in 2018 during a 3-month period between  
167 early April and early July, and thus our work represents a postmortem investigation into the drivers of  
168 cumulative tree mortality through the course of the hot drought.

169 Following the call by Wyngaard et al. (2019), we establish “data product levels” to reflect the image processing  
170 pipeline from raw imagery (Level 0) to calibrated, fine-scale forest structure and composition information on  
171 regular grids (Level 4), with each new data level derived from levels below it. Here, we outline the steps in the  
172 processing and calibration pipeline visualized in Figure 2, and include additional details in the Supplemental  
173 Information.

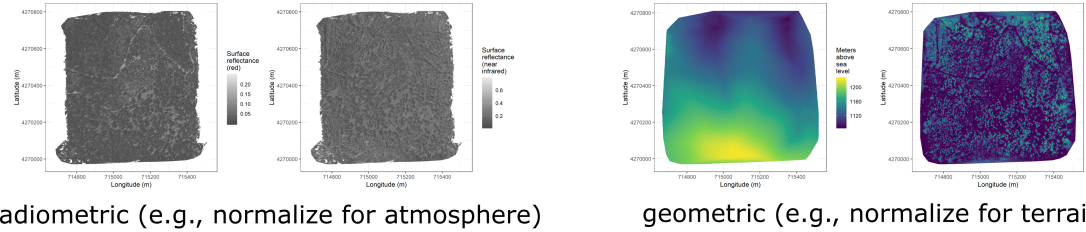
## Level 0: raw data from sensors



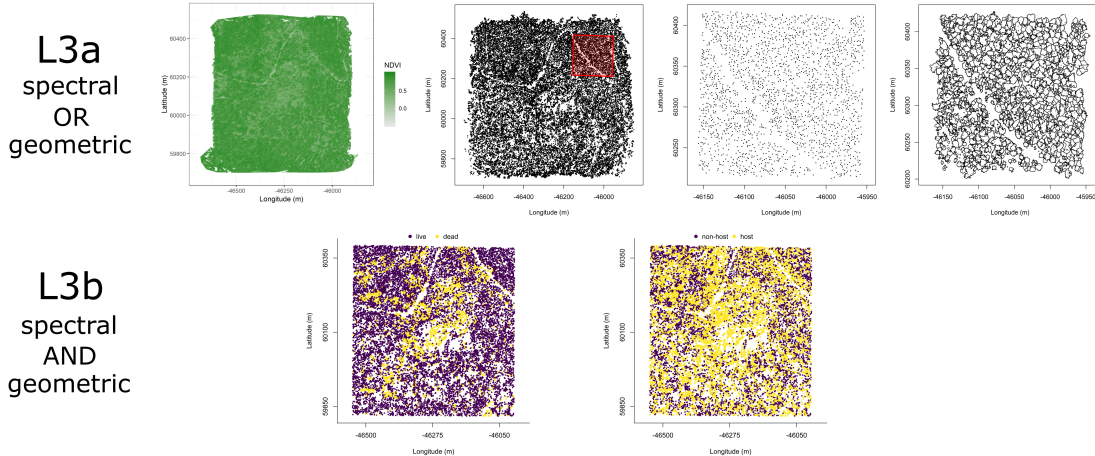
## Level 1: basic outputs from photogrammetric processing



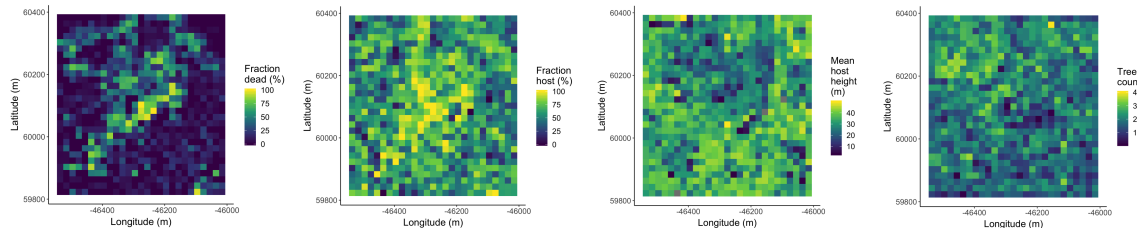
## Level 2: corrected outputs from photogrammetric processing



## Level 3: domain-specific information extraction



## Level 4: aggregations to regular grids



175 Figure 2. Schematic of the data processing workflow for a single site with each new data product level derived  
176 from data at lower levels.

177 Level 0 represents raw data from the sensors. From left to right: example broad-band RGB photo from  
178 DJI Zenmuse X3 camera, example blue photo from Rededge3 (centered on 475nm), example green photo  
179 from Rededge3 (centered on 560nm), example red photo from Rededge3 (centered on 668nm), example near  
180 infrared photo from Rededge3 (centered on 840nm), and example red edge photo from Rededge3 (centered on  
181 717nm).

182 Level 1 represents basic outputs from the photogrammetric workflow, in this case implemented with  
183 Pix4Dmapper. From left to right: a dense point cloud visualized in CloudCompare (<https://www.danielgm.net/cc/>), an orthophoto generated from the RGB camera, and a digital surface model representing the  
184 altitude above sea level (ground height + vegetation height) for every cell.  
185

186 Level 2 represents outputs from photogrammetric processing that have been corrected radiometrically or  
187 geometrically. From left to right: a radiometrically-corrected surface reflectance map of the red narrow band  
188 from the Rededge3 camera, a radiometrically-corrected surface reflectance map of the near infrared narrow  
189 band from the Rededge3 camera, a rasterized version of the digital terrain model derived by a geometric  
190 correction of the dense point cloud, and a canopy height model derived by subtracting the terrain height  
191 from the digital surface model.

192 Level 3 represents domain-specific information extraction from Level 2 products and is divided into two  
193 sub-levels. Level 3a products are derived using only spectral or only geometric data. From left to right: a  
194 reflectance map of Normalized Difference Vegetation Index (NDVI; Rouse et al. (1973)) derived using the red  
195 and near infrared Level 2 reflectance products, a map of points representing detected trees from the canopy  
196 height model with a red polygon highlighting the area presented in more detail for the next two images, a  
197 close-up of points representing detected trees, and a close-up of polygons representing segmented tree crowns.

198 Level 3b products are derived using both spectral and geometric data. From left to right: a map of the point  
199 locations of detected trees that have been classified as alive or dead based on the pixel values within each  
200 segmented tree crown and a map of the point locations of detected trees classified to WPB host/non-host  
201 using the same spectral information. Note that our study relies on the generation of Level 3a products in  
202 order to combine them and create Level 3b products, but this need not be the case. For instance, deep  
203 learning/neural net methods may be able to use both the spectral and geometric information from Level 2  
204 simultaneously to locate and classify trees in a scene and directly generate Level 3b products without a need  
205 to first generate the Level 3a products shown in this schematic (Weinstein et al. 2019, dos Santos et al. 2019).

206 Level 4 represents aggregations of Level 3 products to regular grids which might better reflect the grain size  
207 of the data for which we have the best calibration and thus the most confidence or which might provide  
208 new information not possible at an individual-tree level (e.g., average distance between trees in a small  
209 neighborhood). From left to right: aggregation of live/dead classified trees as fraction of dead trees in a 20 x  
210 20-m cell, aggregation of host/non-host classified trees as fraction of hosts in a 20 x 20-m cell, aggregation of  
211 mean host height in a 20 x 20-m cell, and aggregation of tree count (including all species), in a 20 x 20-m  
212 cell. In our case, the 20 x 20-m aggregation produces a grid cell with an area of 400 m<sup>2</sup>, which most closely  
213 matches the 404-m<sup>2</sup> area of the ground-based vegetation plots whose data we used in an aggregated form to  
214 calibrate our derivation of Level 3 products.

## 215 **Level 0: Raw data from sensors**

216 Raw data comprised approximately 1900 images per camera lens (one broad-band RGB lens and five narrow-  
217 band multispectral lenses) for each of the 32 sites (Figure 2; Level 0). Prior to the aerial survey, two strips of  
218 bright orange drop cloth (~100 x 15 cm) were positioned as an “X” over the permanent monuments marking  
219 the center of the 5 field plots from Fettig et al. (2019) (see Supplemental Information).

220 We preprogrammed north-south aerial transects using Map Pilot for DJI on iOS flight software (Drones-  
221 MadeEasy 2018) at an altitude of 120 m above ground level (with “ground” defined using a 1-arc-second  
222 digital elevation model (Farr et al. 2007)). The resulting ground sampling distance was approximately 5  
223 cm/px for the Zenmuse X3 RGB camera and approximately 8 cm/px for the Rededge3 multispectral camera.  
224 We used 91.6% image overlap (both forward and side) at the ground for the Zenmuse X3 RGB camera and  
225 83.9% overlap (forward and side) for the Rededge3 multispectral camera.

## 226 **Level 1: Basic outputs from photogrammetric processing**

227 We used SfM photogrammetry implemented in Pix4Dmapper Cloud ([www.pix4d.com](http://www.pix4d.com)) to generate dense point  
228 clouds (Figure 2; Level 1, left), orthophotos (Figure 2; Level 1, center), and digital surface models (Figure 2;  
229 Level 1, right) for each field site (Frey et al. 2018). For 29 sites, we processed the Rededge3 multispectral  
230 imagery alone to generate these products. For three sites, we processed the RGB and the multispectral  
231 imagery together to enhance the point density of the dense point cloud. All SfM projects resulted in a single  
232 processing “block,” indicating that all images in the project were optimized and processed together. The  
233 dense point cloud represents x, y, and z coordinates as well as the color of millions of points per site. The  
234 orthophoto represents a radiometrically uncalibrated, top-down view of the survey site that preserves the  
235 relative x-y positions of objects in the scene. The digital surface model is a rasterized version of the dense

236 point cloud that shows the altitude above sea level for each pixel in the scene at the ground sampling distance  
237 of the camera that generated the Level 0 data.

238 **Level 2: Corrected outputs from photogrammetric processing**

239 **Radiometric corrections**

240 A radiometrically-corrected reflectance map (Figure 2; Level 2, left two figures; i.e., a corrected version of the  
241 Level 1 orthophoto) was generated using the Pix4D software by incorporating incoming light conditions for  
242 each narrow band of the Rededge3 camera (captured simultaneously with the Rededge3 camera using an  
243 integrated downwelling light sensor) as well as a pre-flight image of a calibration panel of known reflectance  
244 (see Supplemental Information for camera and calibration panel details).

245 **Geometric corrections**

246 We implemented a geometric correction to the Level 1 dense point cloud and digital surface model by  
247 normalizing these data for the terrain underneath the vegetation. We generated the digital terrain model  
248 representing the ground underneath the vegetation at 1-m resolution (Figure 2; Level 2, third image) by  
249 classifying each survey area’s dense point cloud into “ground” and “non-ground” points using a cloth simulation  
250 filter algorithm (Zhang et al. 2016) implemented in the `lidR` (Roussel et al. 2019) package and rasterizing  
251 the ground points using the `raster` package (Hijmans et al. 2019). We generated a canopy height model  
252 (Figure 2; Level 2, fourth image) by subtracting the digital terrain model from the digital surface model.

253 **Level 3: Domain-specific information extraction**

254 **Level 3a: Data derived from spectral OR geometric Level 2 product**

255 Using just the spectral information from the radiometrically-corrected reflectance maps, we calculated several  
256 vegetation indices including the normalized difference vegetation index (NDVI; Rouse et al. (1973); Figure  
257 2; Level 3a, first image), the normalized difference red edge (NDRE; Gitelson and Merzlyak (1994)), the  
258 red-green index (RGI; Coops et al. (2006)), the red edge chlorophyll index ( $CI_{red\ edge}$ ; Clevers and Gitelson  
259 (2013)), and the green chlorophyll index ( $CI_{green}$ ; Clevers and Gitelson (2013)).

Table 1: Algorithm name, number of parameter sets tested for each algorithm, and references.

Algorithm	Parameter sets tested	Reference(s)
li2012	131	Li et al. (2012); Jakubowski et al. (2013); Shin et al. (2018)

Algorithm	Parameter sets tested	Reference(s)
lmfx	30	Roussel (2019)
localMaxima	6	Roussel et al. (2019)
multichm	1	Eysn et al. (2015)
ptrees	3	Vega et al. (2014)
vwf	3	Plowright (2018)
watershed	3	Pau et al. (2010)

Using just the geometric information from the canopy height model or terrain-normalized dense point cloud, we generated maps of detected trees (Figure 2; Level 3a, second and third images) by testing a total of 7 automatic tree detection algorithms and a total of 177 parameter sets (Table 1). We used the field plot data to assess each tree detection algorithm/parameter set by converting the distance-from-center and azimuth measurements of the trees in the field plots to x-y positions relative to the field plot centers distinguishable in the Level 2 reflectance maps as the orange fabric X's that we laid out prior to each flight. In the reflectance maps, we located 220 out of 160 field plot centers while some plot centers were obscured due to dense interlocking tree crowns or because a plot center was located directly under a single tree crown. For each of the 220 field plots with identifiable plot centers— the “validation field plots”, we calculated 7 forest structure metrics using the ground data collected by Fettig et al. (2019): total number of trees, number of trees greater than 15 m in height, mean height of trees, 25<sup>th</sup> percentile tree height, 75<sup>th</sup> percentile tree height, mean distance to nearest tree neighbor, and mean distance to second nearest neighbor. For each tree detection algorithm and parameter set described above, we calculated the same set of 7 structure metrics within the footprint of the validation field plots. We calculated the Pearson’s correlation and root mean square error (RMSE) between the ground data and the aerial data for each of the 7 structure metrics for each of the 177 automatic tree detection algorithms/parameter sets. For each algorithm and parameter set, we calculated its performance relative to other algorithms as whether its Pearson’s correlation was within 5% of the highest Pearson’s correlation as well as whether its RMSE was within 5% of the lowest RMSE. We summed the number of forest structure metrics for which it reached these 5% thresholds for each algorithm/parameter set. For automatically detecting trees across the whole study, we selected the algorithm/parameter set that performed well across the most number of forest metrics (see Results).

We delineated individual tree crowns (Figure 2; Level 3a, fourth image) with a marker controlled watershed segmentation algorithm (Meyer and Beucher 1990) implemented in the **ForestTools** package (Plowright

283 2018) using the detected treetops as markers. If the automatic segmentation algorithm failed to generate  
284 a crown segment for a detected tree (e.g., often snags with a very small crown footprint), a circular crown  
285 was generated with a radius of 0.5 m. If the segmentation generated multiple polygons for a single detected  
286 tree, only the polygon containing the detected tree was retained. Because image overlap decreases near the  
287 edges of the overall flight path and reduces the quality of the SfM processing in those areas, we excluded  
288 segmented crowns within 35 m of the edge of the survey area. Given the narrower field of view of the  
289 Rededge3 multispectral camera versus the X3 RGB camera whose optical parameters were used to define the  
290 ~40 hectare survey area around each site, as well as the 35 m additional buffering, the survey area at each  
291 site was ~30 ha (see Supplemental Information).

### 292 **Level 3b: Data derived from spectral AND geometric information**

293 We overlaid the segmented crowns on the reflectance maps from 20 sites spanning the latitudinal and elevation  
294 gradient in the study. Using QGIS (<https://qgis.org/en/site/>), we hand classified 564 trees as live/dead  
295 (Figure 3) and as one of 5 dominant species in the study area (ponderosa pine, *Pinus lambertiana*, *Abies*  
296 *concolor*, *Calocedrus decurrens*, or *Quercus kelloggii*) using the mapped ground data as a guide. Each tree was  
297 further classified as “host” for ponderosa pine or “non-host” for all other species (Fettig 2016). We extracted  
298 all the pixel values within each segmented crown polygon from the five, Level 2 orthorectified reflectance  
299 maps (one per narrow band on the Rededge3 camera) as well as from the five, Level 3a vegetation index  
300 maps using the *velox* package (Hunziker 2017). For each crown polygon, we calculated the mean value of  
301 the extracted Level 2 and Level 3a pixels and used them as ten independent variables in a five-fold cross  
302 validated boosted logistic regression model to predict whether the hand classified trees were alive or dead.  
303 For just the living trees, we similarly used all 10 mean reflectance values per crown polygon to predict tree  
304 species using a five-fold cross validated regularized discriminant analysis. The boosted logistic regression and  
305 regularized discriminant analysis were implemented using the *caret* package in R (Kuhn 2008). Finally, we  
306 used these models to classify all tree crowns in the data set as alive or dead (Figure 2; Level 3b, first image)  
307 as well as the species of living trees (Figure 2; Level 3b, second image).

### 308 **Level 4: Aggregations to regular grids**

309 We rasterized the forest structure and composition data at a spatial resolution similar to that of the field  
310 plots to better match the grain size at which we validated the automatic tree detection algorithms. In each  
311 raster cell, we calculated: number of dead trees, number of ponderosa pine trees, total number of trees, and  
312 mean height of ponderosa pine trees. The values of these variables in each grid cell and derivatives from  
313 them were used for visualization and modeling. Here, we show the fraction of dead trees per cell (Figure 2;

314 Level 4, first image), the fraction of host trees per cell (Figure 2; Level 4, second image), the mean height of  
315 ponderosa pine trees in each cell (Figure 2; Level 4, third image), and the total count of trees per cell (Figure  
316 2; Level 4, fourth image).

317 **Note on assumptions about dead trees**

318 For the purposes of this study, we assumed that all dead trees were ponderosa pine and thus hosts colonized  
319 by WPB. This is a reasonably good assumption for our study area; for example, Fettig et al. (2019) found  
320 that 73.4% of dead trees in their coincident field plots were ponderosa pine. Mortality was concentrated in  
321 the larger-diameter classes and attributed primarily to WPB (see Figure 5 of Fettig et al. 2019). The species  
322 contributing to the next highest proportion of dead trees was incense cedar which represented 18.72% of the  
323 dead trees in the field plots. While the detected mortality is most likely to be ponderosa pine killed by WPB,  
324 it is critical to interpret our results with these limitations in mind.

325 **Environmental data**

326 We used CWD (Stephenson 1998) from the 1981-2010 mean value of the basin characterization model (Flint  
327 et al. 2013) as an integrated measure of temperature and moisture conditions for each of the 32 sites. Higher  
328 values of CWD correspond to hotter, drier conditions and lower values correspond to cooler, wetter conditions.  
329 CWD has been shown to correlate well with broad patterns of tree mortality in the Sierra Nevada (Young  
330 et al. 2017) as well as bark beetle-induced tree mortality (Millar et al. 2012). The forests along the entire  
331 CWD gradient used in this study experienced exceptional hot drought between 2012 to 2015 (Griffin and  
332 Anchukaitis 2014, Robeson 2015). We converted the CWD value for each site into a z-score representing that  
333 site's deviation from the mean CWD across the climatic range of Sierra Nevada ponderosa pine as determined  
334 from 179 herbarium records described in Baldwin et al. (2017). Thus, a CWD z-score of 1 would indicate  
335 that the CWD at that site is one standard deviation hotter/drier than the mean CWD across all geolocated  
336 herbarium records for ponderosa pine in the Sierra Nevada.

337 **Statistical model**

338 We used a generalized linear model with a zero-inflated binomial response and a logit link to predict the  
339 probability of ponderosa pine mortality within each 20 x 20-m cell using the total number of ponderosa  
340 pine trees in each cell as the number of trials, and the number of dead trees in each cell as the number of  
341 "successes". As covariates, we used the proportion of trees that are WPB hosts (i.e., ponderosa pine) in each  
342 cell, the mean height of ponderosa pine trees in each cell, the count of trees of all species (overall density) in  
343 each cell, and the site-level CWD using Eq. 1. Note that the two-way interaction between the overall density

344 and the proportion of trees that are hosts is directly proportional to the number of ponderosa pine trees in  
 345 the cell. We centered and scaled all predictor values, and used weakly-regularizing default priors from the  
 346 `brms` package (Bürkner 2017). To measure and account for spatial autocorrelation underlying ponderosa pine  
 347 mortality, we subsampled the data at each site to a random selection of 200, 20 x 20-m cells representing  
 348 approximately 27.5% of the surveyed area. Additionally with these subsampled data, we included a separate  
 349 exact Gaussian process term per site of the noncentered/nonscaled interaction between the x- and y-position  
 350 of each cell using the `gp()` function in the `brms` package (Bürkner 2017). The Gaussian process estimates the  
 351 spatial covariance in the response variable (log-odds of ponderosa pine mortality) jointly with the effects of  
 352 the other covariates.

$$y_{i,j} \sim \begin{cases} 0, & p \\ Binom(n_i, \pi_i), & 1 - p \end{cases}$$

$$\begin{aligned} logit(\pi_i) = & \beta_0 + \\ & \beta_1 X_{cwd,j} + \beta_2 X_{propHost,i} + \beta_3 X_{PIPOheight,i} + \beta_4 X_{overallDensity,i} + \\ & \beta_5 X_{cwd,j} X_{PIPOheight,i} + \beta_6 X_{cwd,j} X_{propHost,i} + \beta_7 X_{cwd,j} X_{overallDensity,i} + \\ & \beta_8 X_{propHost,i} X_{PIPOheight,i} + \beta_9 X_{propHost,i} X_{overallDensity,i} + \\ & \beta_{10} X_{cwd,j} X_{propHost,i} X_{PIPOheight,i} + \\ & \mathcal{GP}_j(x_i, y_i) \end{aligned}$$

353 Where  $y_i$  is the number of dead trees in cell  $i$ ,  $n_i$  is the sum of the dead trees (assumed to be ponderosa pine)  
 354 and live ponderosa pine trees in cell  $i$ ,  $\pi_i$  is the probability of ponderosa pine tree mortality in cell  $i$ ,  $p$  is  
 355 the probability of there being zero dead trees in a cell arising as a result of an unmodeled process,  $X_{cwd,j}$   
 356 is the z-score of CWD for site  $j$ ,  $X_{propHost,i}$  is the scaled proportion of trees that are ponderosa pine in  
 357 cell  $i$ ,  $X_{PIPOheight,i}$  is the scaled mean height of ponderosa pine trees in cell  $i$ ,  $X_{overallDensity,i}$  is the scaled  
 358 density of all trees in cell  $i$ ,  $x_i$  and  $y_i$  are the x- and y- coordinates of the centroid of the cell in an EPSG3310  
 359 coordinate reference system, and  $\mathcal{GP}_j$  represents the exact Gaussian process describing the spatial covariance  
 360 between cells at site  $j$ .

361 We fit this model using the `brms` package (Bürkner 2017) which implements the No U-Turn Sampler extension  
 362 to the Hamiltonian Monte Carlo algorithm (Hoffman and Gelman 2014) in the Stan programming language  
 363 (Carpenter et al. 2017). We used 4 chains with 4000 iterations each (2000 warmup, 2000 samples), and  
 364 confirmed chain convergence by ensuring all `Rhat` values were less than 1.1 (Brooks and Gelman 1998) and

365 that the bulk and tail effective sample sizes (ESS) for each estimated parameter were greater than 100 times  
366 the number of chains (i.e., greater than 400 in our case). We used posterior predictive checks to visually  
367 confirm model performance by overlaying the density curves of the predicted number of dead trees per cell  
368 over the observed number (Gabry et al. 2019). For the posterior predictive checks, we used 50 random  
369 samples from the model fit to generate 50 density curves and ensured curves were centered on the observed  
370 distribution, paying special attention to model performance at capturing counts of zero.

### 371 Software and data availability

372 All data are available via the Open Science Framework. Statistical analyses were performed using the **brms**  
373 packages. With the exception of the SfM software (Pix4Dmapper Cloud) and the GIS software QGIS, all  
374 data carpentry and analyses were performed using R (R Core Team 2018).

## 375 Results

### 376 Tree detection algorithm performance

377 We found that the experimental **lmfx** algorithm with parameter values of **dist2d = 1** and **ws = 2.5** (Roussel  
378 et al. 2019) performed the best across 7 measures of forest structure as measured by Pearson's correlation  
379 with ground data (Table 2).

Table 2: Correlation and differences between the best performing tree detection algorithm (**lmfx** with **dist2d = 1** and **ws = 2.5**) and the ground data. An asterisk next to the correlation or RMSE indicates that this value was within 5% of the value of the best-performing algorithm/parameter set. Ground mean represents the mean value of the forest metric across the 220 field plots that were visible from the sUAS-derived imagery. The median error is calculated as the median of the differences between the air and ground values for the 220 visible plots. Thus, a positive number indicates an overestimate by the sUAS workflow and a negative number indicates an underestimate.

Forest structure metric	Ground mean	Correlation with ground	RMSE	Median error
total tree count	19	0.67*	8.68*	2
count of trees > 15 m	9.9	0.43	7.38	0
distance to 1st neighbor (m)	2.8	0.55*	1.16*	0.26
distance to 2nd neighbor (m)	4.3	0.61*	1.70*	0.12
height (m); 25 <sup>th</sup> percentile	12	0.16	8.46	-1.2
height (m); mean	18	0.29	7.81*	-2.3
height (m); 75 <sup>th</sup> percentile	25	0.35	10.33*	-4

380 **Classification accuracy for live/dead and host/non-host**

381 The accuracy of live/dead classification on a withheld test dataset was 97.3%. The accuracy of species  
382 classification on a withheld testing dataset was 66.7%. The accuracy of WPB host/non-WPB-host (i.e.,  
383 ponderosa pine versus other tree species) on a withheld testing dataset was 74.4%.

384 **Site summary based on best tree detection algorithm and classification**

385 Across all study sites, we detected, segmented, and classified 452,413 trees (see Supplemental Information for  
386 site summaries). Of these trees, we classified 118,879 as dead (26.3% mortality). Estimated site-level tree  
387 mortality ranged from 6.8% to 53.6%.

388 **Effect of local structure and regional climate on tree mortality attributed to western pine  
389 beetle**

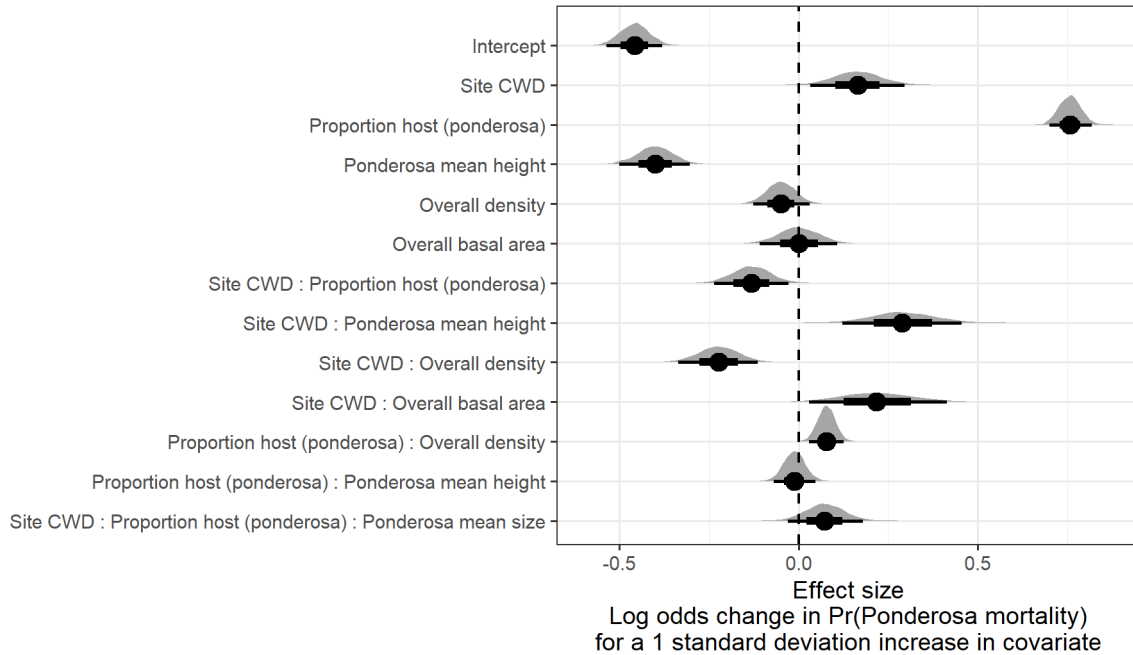


Figure 4: Posterior distributions of effect size from zero-inflated binomial model predicting the probability of ponderosa pine mortality in a 20 x 20-m cell given forest structure characteristics and site-level climatic water deficit (CWD). The gray density distribution for each model covariate represents the density of the posterior distribution, the point underneath each density curve represents the median of the estimate, the bold interval surrounding the point estimate represents the 66% credible interval, and the thin interval surrounding the point estimate represents the 95% credible interval.

390 We detected a positive main effect of CWD on the probability of ponderosa pine mortality within each 20  
391 x 20-m cell (Figure 4). We found a positive main effect of proportion of host trees per cell, with a greater  
392 proportion of host trees (i.e., ponderosa pine) in a cell increasing the probability of ponderosa pine mortality.

393 Conversely, we found a negative effect of overall tree density (i.e., including both ponderosa pine and non-host  
394 species) such that greater tree density in a 20 x 20-m cell (for the same proportion of host trees) would  
395 decrease the probability of ponderosa pine mortality. We found a positive two-way interaction between the  
396 overall tree density per cell and the proportion of trees that were hosts, which is equivalent to a positive  
397 effect of the density of host trees (Figure 4).

398 We found a negative effect of mean height of ponderosa pine on the probability of ponderosa mortality,  
399 suggesting that WPB attacked smaller trees, on average. However, there was a positive interaction between  
400 CWD and ponderosa pine mean height, such that larger trees were more likely to increase the probability of  
401 ponderosa mortality in hotter, drier sites (Figure 5).

402 We found weakly negative effects of the site-level CWD interactions with both the proportion of host trees  
403 and overall tree density (Figure 4).

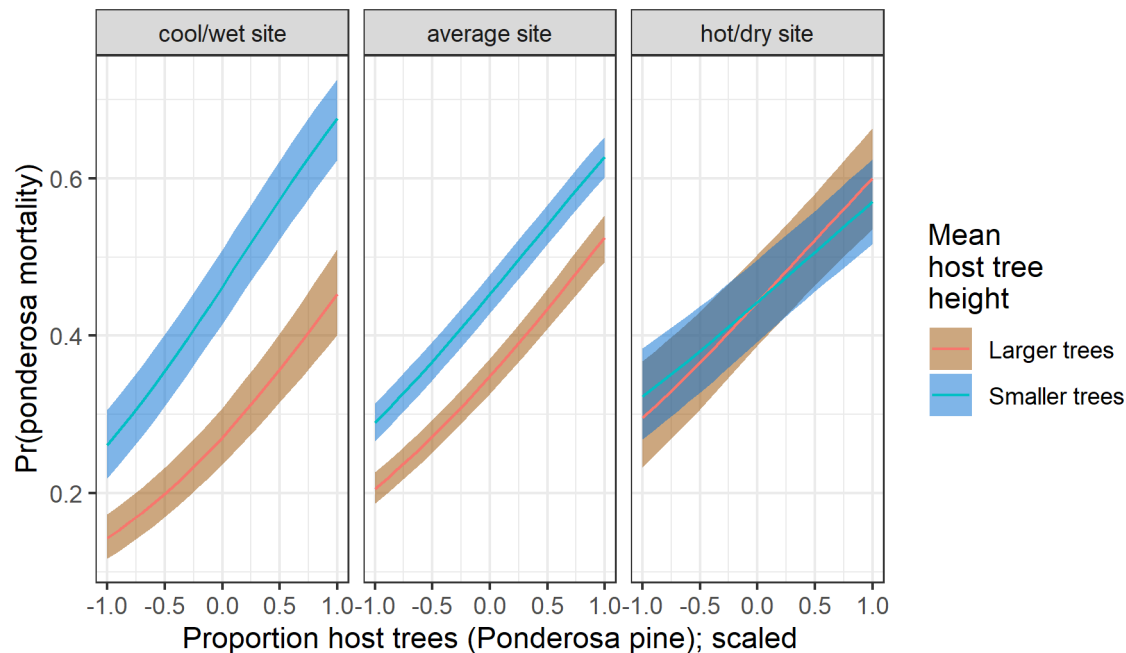


Figure 5: Line version of model results with 95% credible intervals showing primary influence of ponderosa pine structure on the probability of ponderosa pine mortality, and the interaction across climatic water deficit. The ‘larger trees’ line represents the mean height of ponderosa pine 0.7 standard deviations above the mean (approximately 24.1 m), and the ‘smaller trees’ line represents the mean height of ponderosa pine 0.7 standard deviations below the mean (approximately 12.1 m).

## 404 Discussion

405 This study represents a novel use of drones to further our understanding of the simultaneous effects of  
406 local forest structure and composition with broad-scale environmental gradients on tree mortality attributed

407 to WPB. We found strong positive effects (effect sizes >0.4) of both the proportion of host trees and the  
408 interaction between site CWD and host tree mean size (height) on the probability of ponderosa pine mortality.  
409 Conversely, we found a strong negative effect (effect size <-0.4) of mean height of ponderosa pine. Site-level  
410 CWD exerted a positive, but relatively weak, main effect on the probability of ponderosa mortality (effect  
411 size: 0.16; 95% CI: [0.03, 0.30]). To that end, we did not measure tree water stress at an individual tree level  
412 as in other recent work (Stephenson et al. 2019), and instead treated CWD as a general indicator of tree  
413 stress following results of coarser-scale studies (e.g., Asner et al. 2016, Young et al. 2017), which may have  
414 contributed to our failure to detect a stronger CWD effect. Also, our entire study area experienced the same  
415 extreme hot drought between 2012 and 2015 and the variation of mortality explained by a main effect of  
416 CWD may be dampened when most trees are experiencing a high degree of water stress (Floyd et al. 2009,  
417 Fettig et al. 2019).

418 **Positive effect of host density and a negative effect of overall density**

419 The strongest effect on the probability of ponderosa pine mortality was the positive effect of the proportion  
420 of trees in each 20 x 20-m cell that were ponderosa pine– the host of the WPB (effect size: 0.76; 95% CI:  
421 [0.70, 0.82]).

422 A number of mechanisms associated with the relative abundance of species in a local area might underlie  
423 this relationship. Frequency-dependent herbivory—whereby mixed-species forests experience less herbivory  
424 compared to monocultures (as an extreme example)—is common, especially for oligophagous insect species  
425 (Jactel and Brockerhoff 2007). Furthermore, it has been demonstrated that nonhost volatiles reduce attraction  
426 of several species of bark beetles to their aggregation pheromones (Seybold et al. 2018), including WPB  
427 (Fettig et al. 2005). To that end, combinations of nonhost volatiles and an antiaggregation pheromone have  
428 been used successfully to reduce levels of tree mortality attributed to WPB (e.g., Fettig et al. 2012). In  
429 general, Hayes et al. (2009) and Fettig et al. (2019) found that measures of host availability explained less  
430 variation in mortality than measures of overall tree density, but those conclusions were based on a response  
431 variable of “total number of dead host trees,” rather than the number of dead host trees conditional on the  
432 total number of host trees as in our study (i.e., a binomial response).

433 The negative relationship between overall tree density, a potential correlate of the local competitive envi-  
434 ronment, and the probability of ponderosa pine mortality is counter-intuitive but corroborates findings of  
435 coincident ground plots (Fettig et al. 2019, in their analysis using proportion of trees killed as a response)  
436 and other work during the same hot drought (Restaino et al. 2019). In the absence of management, the forest  
437 structure is itself a product of climate and, with increasing importance at finer spatial scales, topographic

438 conditions (Fricker et al. 2019). Thus, the denser forest patches in our study may indicate greater local  
439 water availability, more favorable conditions for tree growth and survivorship, and increased resistance to  
440 beetle-induced mortality (Restaino et al. 2019). The negative two-way interaction between site CWD and  
441 overall density that amplifies the negative overall density effect in hotter, drier sites (effect size: -0.22; 95%  
442 CI: [-0.34, -0.11]) supports this explanation if greater local tree density implies especially favorable growing  
443 conditions (and locally resistant trees) when denser patches are found in hot, dry sites.

444 We found a positive two-way interaction between overall tree density (host and non-host) within each cell  
445 and proportion of host trees, which is equivalent to a positive effect of host density (effect size: 0.08; 95% CI:  
446 [0.03, 0.13]). The relationship between host density and susceptibility to colonization by bark beetles has  
447 been so well-documented at the experimental plot level (e.g., Raffa and Berryman 1987, Oliver 1995) that  
448 lowering stand densities through selective harvest of hosts is commonly recommended for reducing future  
449 levels of tree mortality attributed to bark beetles (Fettig and Hilszczański 2015), including WPB (Fettig  
450 2016). Greater host density shortens the flight distance required for WPB to disperse to new hosts, which  
451 likely facilitates bark beetle spread, however we calibrated our aerial tree detection to ~400 m<sup>2</sup> areas rather  
452 than to individual tree locations, so our data are insufficient to address these relationships. Increased density  
453 of ponderosa pine, specifically, may disproportionately increase the competitive environment for host trees  
454 (and thus increase their susceptibility to WPB colonization) if intraspecific competition amongst ponderosa  
455 pine trees is stronger than interspecific competition as would be predicted with coexistence theory (Chesson  
456 2000). Finally, greater host densities increase the frequency that searching WPB land on hosts, rather than  
457 nonhosts, thus reducing the amount of energy expended during host finding and selection as well as the time  
458 that searching WPB spend exposed to predators.

#### 459 **Negative main effect of host tree mean size, but strong positive interaction with site CWD**

460 Counter to our expectations, we found an overall negative effect of host tree mean size on the probability of  
461 host mortality (effect size: -0.40; 95% CI: [-0.50, -0.30]). WPB exhibit a preference for trees 50.8 to 76.2  
462 cm in diameter at breast height (Person 1928, 1931), and a positive relationship between host tree size and  
463 levels of tree mortality attributed to WPB was reported by Fettig et al. (2019) in the coincident field plots  
464 as well as in other recent studies (Restaino et al. 2019, Stephenson et al. 2019, Pile et al. 2019). Indeed,  
465 Fettig et al. (2019) reported no mortality in ponderosa pine trees <10.0 cm DBH attributable to WPB and  
466 found no tree size/mortality relationship for incense cedar or white fir in the coincident field plots. These  
467 species represent 22.3% of the total tree mortality observed in their study, yet in our study all dead trees  
468 were classified as ponderosa pine (see Methods) which could dampen positive effect of tree size on mortality.

469 Larger trees are more nutritious and are therefore ideal targets if local bark beetle density is high enough  
470 to successfully initiate mass attack as can occur when many trees are under severe water stress (Bentz et  
471 al. 2010, Kolb et al. 2016). In the recent hot drought, we expected that most trees would be under severe  
472 water stress, setting the stage for increasing beetle density, successful mass attacks, and targeting of larger  
473 trees. A possible explanation for our finding counter to this expectation is that our observations represent the  
474 cumulative mortality of trees during a multi-year drought event and its aftermath. Lower host tree mean size  
475 led to a greater probability of host mortality earlier in this drought (Pile et al. 2019, Stovall et al. 2019) and  
476 that signal might have persisted even as mortality continued to accumulate driven by other factors. Finally,  
477 tree growth rates may be a better predictor of susceptibility to WPB colonization than tree size per se, with  
478 slower-growing trees being most vulnerable (Miller and Keen 1960). While slow-growing trees are often also  
479 the largest trees, this may not be the case for our study sites especially given the legacy of fire exclusion  
480 in the Sierra Nevada and its effect of perturbing forest structure far outside its natural range of variation  
481 (Safford and Stevens 2017).

482 We did observe a strong host tree size effect in its interaction with site CWD (effect size: 0.29; 95% CI: [0.12,  
483 0.46]). In hot, dry sites, larger average host size increased the probability of host mortality while smaller host  
484 sizes increased the probability of host mortality in cooler, wetter sites. Notably, a similar pattern was shown  
485 by Stovall et al. (2019) with a strong positive tree height/mortality relationship in areas with the greatest  
486 vapor pressure deficit and no tree height/mortality relationship in areas with the lowest vapor pressure  
487 deficit. Stovall et al. (2019) did not observe that this environmental dependence extended to a negative tree  
488 height/mortality relationship (as we did) even at the lowest extremes of their vapor pressure deficit gradient,  
489 perhaps because their entire study took place in the southern Sierra Nevada which represents a hotter, drier  
490 portion of the more spatially extensive results we present here. Our work suggests that the WPB was cueing  
491 into different aspects of forest structure across an environmental gradient in a spatial context in a parallel  
492 manner to the temporal context noted by Stovall et al. (2019) and Pile et al. (2019), who observed that  
493 mortality was increasingly driven by larger trees as the hot drought proceeded and became more severe.

494 All of our sites were considered in an “epidemic” population phase for WPB ( $>5$  trees killed per hectare; see  
495 Supplemental Information; Miller and Keen 1960, Hayes et al. 2009), but our results challenge the notion that  
496 outbreak behavior by the WPB and subsequent tree mortality is always driven by greater tree size. Despite a  
497 strong tree size/mortality relationship in coincident ground plots across our study area (Fettig et al. 2019),  
498 our results from surveying the broader context surrounding those ground plots reveals different effects of  
499 host tree size depending on CWD. Thus, it is possible that the massive tree mortality in hotter/drier Sierra  
500 Nevada forests (lower latitudes and elevations; Asner et al. 2016, Young et al. 2017) during the 2012 to

501 2015 hot drought arose as a synergistic alignment of environmental conditions and local forest structure that  
502 allowed WPB to successfully colonize large trees, rapidly increase in population size, and expand. Conversely,  
503 our results may suggest that the unexpectedly low mortality in cooler/wetter Sierra Nevada forests compared  
504 to model predictions based on coarser-scale forest structure data (Young et al. 2017) could be explained  
505 by a different WPB response to local forest structure due to a lack of an alignment with favorable climate  
506 conditions.

## 507 **Limitations and future directions**

508 We have demonstrated that drones can be effective means of collecting forest data at multiple, vastly different  
509 spatial scales to investigate a single, multi-scale phenomenon– from meters in between trees, to hundreds  
510 of meters of elevation, to hundreds of thousands of meters of latitude. Some limitations remain but can be  
511 overcome with further refinements in the use of this tool for forest ecology. Most of these limitations arise  
512 from tree detection and classification uncertainty, and thus it was imperative to work with field data for  
513 calibration and uncertainty reporting.

514 The greatest limitation in our study arising from classification uncertainty is in the assumption that all dead  
515 trees were ponderosa pine, which we estimate from coincident field plots is true approximately 73.4% of  
516 the time. Because the forest structure factors influencing the likelihood of individual tree mortality during  
517 the hot drought depended on tree species (Stephenson et al. 2019), we cannot rule out that some of the  
518 ponderosa pine mortality relationships to forest structure that we observed may be partially explained by  
519 those relationships in other species that were misclassified as ponderosa pine using our methods. However,  
520 the overall community composition across our study area was similar (Fettig et al. 2019) and we are able  
521 to reproduce similar forest structure/mortality patterns in drone-derived data when restricting the scope  
522 of analysis to only trees detected in the footprints of the coincident field plots with dramatically different  
523 patterns observed when including data from the forest surrounding the coincident field plots (see Supplemental  
524 information). Thus, we remain confident that the patterns we observed were driven primarily by the dynamic  
525 between WPB and ponderosa pine. While spectral information of foliage could help classify living trees to  
526 species, the species of standing dead trees were not spectrally distinct. This challenge of classifying standing  
527 dead trees to species implies that a conifer forest system with less bark beetle and tree host diversity, such  
528 as mountain pine beetle outbreaks in monocultures of lodgepole pine in the Intermountain West, should be  
529 particularly amenable to the methods presented here even with minimal further refinement because dead  
530 trees will almost certainly belong to a single species and have succumbed to colonization by a single bark  
531 beetle species.

532 Some uncertainty surrounded our ability to detect trees using the geometry of the dense point clouds derived  
533 with SfM. The horizontal accuracy of the tree detection was better than the vertical accuracy, which may  
534 result from a more significant error contribution by the field-based calculations of tree height compared to  
535 tree position relative to plot center (Table 2). Both the horizontal and vertical accuracy would likely improve  
536 with better SfM point clouds, which can be enhanced with greater overlap between images (Frey et al. 2018)  
537 or with oblique (i.e., off-nadir) imagery (James and Robson 2014). Frey et al. (2018) found that 95% overlap  
538 was preferable for generating dense point clouds in forested areas, and James and Robson (2014) reduced  
539 dense point cloud errors using imagery taken at 30 degrees off-nadir. We only achieved 91.6% overlap with  
540 the X3 RGB camera and 83.9% overlap with the multispectral camera, and all imagery was nadir-facing.  
541 While our live/dead classification was fairly accurate (97.3% on a withheld dataset), our species classifier  
542 would likely benefit from better crown segmentation because the pixel-level reflectance values within each  
543 crown are averaged to characterize the “spectral signature” of each tree. With better delineation of each  
544 tree crown, the mean value of pixels within each tree crown will likely be more representative of that tree’s  
545 spectral signature. Better crown segmentation might most readily be achieved through greater overlap in  
546 imagery. Finally, we anticipate that computer vision and deep learning will prove helpful in overcoming some  
547 of these detection and classification challenges (Gray et al. 2019).

## 548 Conclusions

549 Climate change adaptation strategies emphasize management action that considers whole-ecosystem responses  
550 to inevitable change (Millar et al. 2007), which requires a macroecological understanding of how phenomena  
551 at multiple scales can interact. We’ve shown that drones can be a valuable tool for investigating multi-scalar  
552 phenomena, such as how local forest structure combines with environmental conditions to shape forest insect  
553 disturbance. Understanding the conditions that drive dry western U.S. forest responses to disturbances such  
554 as bark beetle outbreaks will be vital for predicting outcomes from increasing disturbance frequency and  
555 intensity exacerbated by climate change. Our study suggests that outcomes will depend on interactions  
556 between local forest structure and broad-scale environmental gradients, with the potential for cross-scale  
557 interactions to challenge our current understanding of forest insect dynamics.

## 558 References

559 Anderegg, W. R. L., J. A. Hicke, R. A. Fisher, C. D. Allen, J. Aukema, B. Bentz, S. Hood, J. W. Lichstein,  
560 A. K. Macalady, N. McDowell, Y. Pan, K. Raffa, A. Sala, J. D. Shaw, N. L. Stephenson, C. Tague, and  
561 M. Zeppel. 2015. Tree mortality from drought, insects, and their interactions in a changing climate. New

- 562 Phytologist 208:674–683.
- 563 Asner, G. P., P. G. Brodrick, C. B. Anderson, N. Vaughn, D. E. Knapp, and R. E. Martin. 2016. Progressive  
564 forest canopy water loss during the 2012–2015 California drought. Proceedings of the National Academy of  
565 Sciences 113:E249–E255.
- 566 Baldwin, B. G., A. H. Thornhill, W. A. Freyman, D. D. Ackerly, M. M. Kling, N. Morueta-Holme, and B. D.  
567 Mishler. 2017. Species richness and endemism in the native flora of California. American Journal of Botany  
568 104:487–501.
- 569 Bedard, W. D., P. E. Tilden, D. L. Wood, R. M. Silverstein, R. G. Brownlee, and J. O. Rodin. 1969.  
570 Western pine beetle: Field response to its sex pheromone and a synergistic host terpene, myrcene. Science  
571 164:1284–1285.
- 572 Bentz, B. J., J. Régnière, C. J. Fettig, E. M. Hansen, J. L. Hayes, J. A. Hicke, R. G. Kelsey, J. F. Negrón,  
573 and S. J. Seybold. 2010. Climate change and bark beetles of the western United States and Canada: Direct  
574 and indirect effects. BioScience 60:602–613.
- 575 Berryman, A. A. 1982. Population dynamics of bark beetles. Pages 264–314 in Bark Beetles in North  
576 American Conifers: A System for the Study of Evolutionary Biology.
- 577 Brooks, S. P., and A. Gelman. 1998. General methods for monitoring convergence of iterative simulations.  
578 Journal of Computational and Graphical Statistics 7:434.
- 579 Bürkner, P.-C. 2017. **brms**: An *R* package for bayesian multilevel models using *Stan*. Journal of Statistical  
580 Software 80:1–28.
- 581 Byers, J. A., and D. L. Wood. 1980. Interspecific inhibition of the response of the bark beetles, *Dendroctonus*  
582 *brevicomis* and *Ips paraconfusus*, to their pheromones in the field. Journal of Chemical Ecology 6:149–164.
- 583 Carpenter, B., A. Gelman, M. D. Hoffman, D. Lee, B. Goodrich, M. Betancourt, M. Brubaker, J. Guo, P. Li,  
584 and A. Riddell. 2017. Stan: A Probabilistic Programming Language. Journal of Statistical Software 76:1–32.
- 585 Chesson, P. 2000. Mechanisms of maintenance of species diversity. Annual Review of Ecology and Systematics  
586 31:343–366.
- 587 Chubaty, A. M., B. D. Roitberg, and C. Li. 2009. A dynamic host selection model for mountain pine beetle,  
588 *Dendroctonus ponderosae* Hopkins. Ecological Modelling 220:1241–1250.
- 589 Clevers, J., and A. Gitelson. 2013. Remote estimation of crop and grass chlorophyll and nitrogen content using  
590 red-edge bands on Sentinel-2 and -3. International Journal of Applied Earth Observation and Geoinformation

- 591 23:344–351.
- 592 Coops, N. C., M. Johnson, M. A. Wulder, and J. C. White. 2006. Assessment of QuickBird high spatial  
593 resolution imagery to detect red attack damage due to mountain pine beetle infestation. *Remote Sensing of*  
594 *Environment* 103:67–80.
- 595 DJI. 2015a. Zenmuse X3 - Creativity Unleashed. <https://www.dji.com/zenmuse-x3/info>.
- 596 DJI. 2015b. DJI - The World Leader in Camera Drones/Quadcopters for Aerial Photography. <https://www.dji.com/matrice100/info>.
- 598 DronesMadeEasy. 2018. Map Pilot for DJI on iOS. [https://itunes.apple.com/us/app/map-pilot-for-dji/  
599 id1014765000?mt=8](https://itunes.apple.com/us/app/map-pilot-for-dji/id1014765000?mt=8).
- 600 Evenden, M. L., C. M. Whitehouse, and J. Sykes. 2014. Factors influencing flight capacity of the mountain  
601 pine beetle (Coleoptera: Curculionidae: Scolytinae). *Environmental Entomology* 43:187–196.
- 602 Eysn, L., M. Hollaus, E. Lindberg, F. Berger, J.-M. Monnet, M. Dalponte, M. Kobal, M. Pellegrini, E.  
603 Lingua, D. Mongus, and N. Pfeifer. 2015. A benchmark of LiDAR-based single tree detection methods using  
604 heterogeneous forest data from the alpine space. *Forests* 6:1721–1747.
- 605 Farr, T. G., P. A. Rosen, E. Caro, R. Crippen, R. Duren, S. Hensley, M. Kobrick, M. Paller, E. Rodriguez, L.  
606 Roth, D. Seal, S. Shaffer, J. Shimada, J. Umland, M. Werner, M. Oskin, D. Burbank, and D. Alsdorf. 2007.  
607 The shuttle radar topography mission. *Reviews of Geophysics* 45.
- 608 Fettig, C. J. 2012. Chapter 2: Forest health and bark beetles. *in* Managing Sierra Nevada Forests. PSW-  
609 GTR-237. USDA Forest Service.
- 610 Fettig, C. J. 2016. Native bark beetles and wood borers in Mediterranean forests of California. Pages 499–528  
611 *in* Insects and diseases of Mediterranean Forest systems. Springer International Publishing, Switzerland.
- 612 Fettig, C. J., and J. Hilszczański. 2015. Management strategies for bark beetles in conifer forests. Pages  
613 555–584 *in* Bark Beetles. Elsevier.
- 614 Fettig, C. J., K. D. Klepzig, R. F. Billings, A. S. Munson, T. E. Nebeker, J. F. Negrón, and J. T. Nowak. 2007.  
615 The effectiveness of vegetation management practices for prevention and control of bark beetle infestations in  
616 coniferous forests of the western and southern United States. *Forest Ecology and Management* 238:24–53.
- 617 Fettig, C. J., S. R. McKelvey, C. P. Dabney, D. P. W. Huber, C. G. Lait, D. L. Fowler, and J. H. Borden. 2012.  
618 Efficacy of “Verbenone Plus” for protecting ponderosa pine trees and stands from *Dendroctonus brevicomis*  
619 (Coleoptera: Curculionidae) attack in British Columbia and California. *Journal of Economic Entomology*

- 620 105:1668–1680.
- 621 Fettig, C. J., S. R. McKelvey, and D. P. W. Huber. 2005. Nonhost angiosperm volatiles and Verbenone disrupt  
622 response of western pine beetle, *Dendroctonus brevicomis* (Coleoptera: Scolytidae), to attractant-baited traps.  
623 Journal of Economic Entomology 98:2041–2048.
- 624 Fettig, C. J., L. A. Mortenson, B. M. Bulaon, and P. B. Fulk. 2019. Tree mortality following drought in the  
625 central and southern Sierra Nevada, California, U.S. Forest Ecology and Management 432:164–178.
- 626 Flint, L. E., A. L. Flint, J. H. Thorne, and R. Boynton. 2013. Fine-scale hydrologic modeling for regional land-  
627 scape applications: The California Basin Characterization Model development and performance. Ecological  
628 Processes 2:25.
- 629 Floyd, M. L., M. Clifford, N. S. Cobb, D. Hanna, R. Delph, P. Ford, and D. Turner. 2009. Relationship of  
630 stand characteristics to drought-induced mortality in three Southwestern piñonJuniper woodlands. Ecological  
631 Applications 19:1223–1230.
- 632 Franceschi, V. R., P. Krokene, E. Christiansen, and T. Krekling. 2005. Anatomical and chemical defenses of  
633 conifer bark against bark beetles and other pests. New Phytologist 167:353–376.
- 634 Frey, J., K. Kovach, S. Stemmler, and B. Koch. 2018. UAV photogrammetry of forests as a vulnerable  
635 process. A sensitivity analysis for a structure from motion RGB-image pipeline. Remote Sensing 10:912.
- 636 Fricker, G. A., N. W. Synes, J. M. Serra-Diaz, M. P. North, F. W. Davis, and J. Franklin. 2019. More than  
637 climate? Predictors of tree canopy height vary with scale in complex terrain, Sierra Nevada, CA (USA).  
638 Forest Ecology and Management 434:142–153.
- 639 Gabry, J., D. Simpson, A. Vehtari, M. Betancourt, and A. Gelman. 2019. Visualization in Bayesian workflow.  
640 Journal of the Royal Statistical Society: Series A (Statistics in Society) 182:389–402.
- 641 Gitelson, A., and M. N. Merzlyak. 1994. Spectral reflectance changes associated with autumn senescence of  
642 *Aesculus hippocastanum* L. And *Acer platanoides* L. Leaves. Spectral features and relation to chlorophyll  
643 estimation. Journal of Plant Physiology 143:286–292.
- 644 Graf, M., M. Reid, B. Aukema, and B. Lindgren. 2012. Association of tree diameter with body size and lipid  
645 content of mountain pine beetles. The Canadian Entomologist 144:467–477.
- 646 Gray, P. C., A. B. Fleishman, D. J. Klein, M. W. McKown, V. S. Bézy, K. J. Lohmann, and D. W. Johnston.  
647 2019. A convolutional neural network for detecting sea turtles in drone imagery. Methods in Ecology and  
648 Evolution 10:345–355.

- 649 Griffin, D., and K. J. Anchukaitis. 2014. How unusual is the 2012-2014 California drought? *Geophysical*  
650 *Research Letters* 41:9017–9023.
- 651 Hayes, C. J., C. J. Fettig, and L. D. Merrill. 2009. Evaluation of multiple funnel traps and stand characteristics  
652 for estimating western pine beetle-caused tree mortality. *Journal of Economic Entomology* 102:2170–2182.
- 653 Hijmans, R. J., J. van Etten, M. Sumner, J. Cheng, A. Bevan, R. Bivand, L. Busetto, M. Canty, D. Forrest,  
654 A. Ghosh, D. Golicher, J. Gray, J. A. Greenberg, P. Hiemstra, I. for M. A. Geosciences, C. Karney, M.  
655 Mattiuzzi, S. Mosher, J. Nowosad, E. Pebesma, O. P. Lamigueiro, E. B. Racine, B. Rowlingson, A. Shortridge,  
656 B. Venables, and R. Wueest. 2019. *Raster: Geographic data analysis and modeling*.
- 657 Hoffman, M. D., and A. Gelman. 2014. The No-U-Turn Sampler: Adaptively setting path lengths in  
658 Hamiltonian Monte Carlo. *Journal of Machine Learning Research* 15:31.
- 659 Hunziker, P. 2017. *Velox: Fast raster manipulation and extraction*.
- 660 Jactel, H., and E. G. Brockerhoff. 2007. Tree diversity reduces herbivory by forest insects. *Ecology Letters*  
661 10:835–848.
- 662 Jakubowski, M. K., W. Li, Q. Guo, and M. Kelly. 2013. Delineating individual trees from LiDAR data: A  
663 comparison of vector- and raster-based segmentation approaches. *Remote Sensing* 5:4163–4186.
- 664 James, M. R., and S. Robson. 2014. Mitigating systematic error in topographic models derived from UAV  
665 and ground-based image networks. *Earth Surface Processes and Landforms* 39:1413–1420.
- 666 Kane, V. R., M. P. North, J. A. Lutz, D. J. Churchill, S. L. Roberts, D. F. Smith, R. J. McGaughey, J. T.  
667 Kane, and M. L. Brooks. 2014. Assessing fire effects on forest spatial structure using a fusion of Landsat and  
668 airborne LiDAR data in Yosemite National Park. *Remote Sensing of Environment* 151:89–101.
- 669 Kolb, T. E., C. J. Fettig, M. P. Ayres, B. J. Bentz, J. A. Hicke, R. Mathiasen, J. E. Stewart, and A. S. Weed.  
670 2016. Observed and anticipated impacts of drought on forest insects and diseases in the United States. *Forest*  
671 *Ecology and Management* 380:321–334.
- 672 Kuhn, M. 2008. Building predictive models in R using the caret package. *Journal of Statistical Software*  
673 28:1–26.
- 674 Larson, A. J., and D. Churchill. 2012. Tree spatial patterns in fire-frequent forests of western North America,  
675 including mechanisms of pattern formation and implications for designing fuel reduction and restoration  
676 treatments. *Forest Ecology and Management* 267:74–92.
- 677 Li, W., Q. Guo, M. K. Jakubowski, and M. Kelly. 2012. A new method for segmenting individual trees from

- 678 the LiDAR point cloud. Photogrammetric Engineering & Remote Sensing 78:75–84.
- 679 Logan, J. A., P. White, B. J. Bentz, and J. A. Powell. 1998. Model analysis of spatial patterns in mountain  
680 pine beetle outbreaks. Theoretical Population Biology 53:236–255.
- 681 Meyer, F., and S. Beucher. 1990. Morphological segmentation. Journal of Visual Communication and Image  
682 Representation 1:21–46.
- 683 Micasense. 2015. MicaSense. <https://support.micasense.com/hc/en-us/articles/215261448-RedEdge-User-Manual-PDF-Download->.
- 685 Millar, C. I., N. L. Stephenson, and S. L. Stephens. 2007. Climate change and forests of the future: Managing  
686 in the face of uncertainty. Ecological Applications 17:2145–2151.
- 687 Millar, C. I., R. D. Westfall, D. L. Delany, M. J. Bokach, A. L. Flint, and L. E. Flint. 2012. Forest mortality in  
688 high-elevation whitebark pine (*Pinus albicaulis*) forests of eastern California, USA: Influence of environmental  
689 context, bark beetles, climatic water deficit, and warming. Canadian Journal of Forest Research 42:749–765.
- 690 Miller, J. M., and F. P. Keen. 1960. Biology and control of the western pine beetle: A summary of the first  
691 fifty years of research. US Department of Agriculture.
- 692 Moeck, H. A., D. L. Wood, and K. Q. Lindahl. 1981. Host selection behavior of bark beetles (Coleoptera:  
693 Scolytidae) attacking *Pinus ponderosa*, with special emphasis on the western pine beetle, *Dendroctonus*  
694 *brevicomis*. Journal of Chemical Ecology 7:49–83.
- 695 Morris, J. L., S. Cottrell, C. J. Fettig, W. D. Hansen, R. L. Sherriff, V. A. Carter, J. L. Clear, J. Clement, R.  
696 J. DeRose, J. A. Hicke, P. E. Higuera, K. M. Mattor, A. W. R. Seddon, H. T. Seppä, J. D. Stednick, and S.  
697 J. Seybold. 2017. Managing bark beetle impacts on ecosystems and society: Priority questions to motivate  
698 future research. Journal of Applied Ecology 54:750–760.
- 699 Oliver, W. W. 1995. Is self-thinning in ponderosa pine ruled by *Dendroctonus* bark beetles? Page 6 in Forest  
700 health through silviculture: Proceedings of the 1995 National Silviculture Workshop.
- 701 Pau, G., F. Fuchs, O. Sklyar, M. Boutros, and W. Huber. 2010. EBImage: An R package for image processing  
702 with applications to cellular phenotypes. Bioinformatics 26:979–981.
- 703 Person, H. L. 1928. Tree selection by the western pine beetle. Journal of Forestry 26:564–578.
- 704 Person, H. L. 1931. Theory in explanation of the selection of certain trees by the western pine beetle. Journal  
705 of Forestry 29:696–699.

- 706 Pile, L. S., M. D. Meyer, R. Rojas, O. Roe, and M. T. Smith. 2019. Drought impacts and compounding  
707 mortality on forest trees in the southern Sierra Nevada. *Forests* 10:237.
- 708 Plowright, A. 2018. ForestTools: Analyzing remotely sensed forest data.
- 709 Raffa, K. F., B. H. Aukema, B. J. Bentz, A. L. Carroll, J. A. Hicke, M. G. Turner, and W. H. Romme. 2008.  
710 Cross-scale drivers of natural disturbances prone to anthropogenic amplification: The dynamics of bark beetle  
711 eruptions. *BioScience* 58:501–517.
- 712 Raffa, K. F., and A. A. Berryman. 1983. The role of host plant resistance in the colonization behavior and  
713 ecology of bark beetles (Coleoptera: Scolytidae). *Ecological Monographs* 53:27–49.
- 714 Raffa, K. F., and A. A. Berryman. 1987. Interacting selective pressures in conifer-bark beetle systems: A  
715 basis for reciprocal adaptations? *The American Naturalist* 129:234–262.
- 716 Raffa, K. F., J.-C. Grégoire, and B. Staffan Lindgren. 2015. Natural history and ecology of bark beetles.  
717 Pages 1–40 in *Bark Beetles*. Elsevier.
- 718 R Core Team. 2018. R: A language and environment for statistical computing. R Foundation for Statistical  
719 Computing, Vienna, Austria.
- 720 Restaino, C., D. Young, B. Estes, S. Gross, A. Wuenschel, M. Meyer, and H. Safford. 2019. Forest  
721 structure and climate mediate drought-induced tree mortality in forests of the Sierra Nevada, USA. *Ecological  
722 Applications* 0:e01902.
- 723 Robeson, S. M. 2015. Revisiting the recent California drought as an extreme value. *Geophysical Research  
724 Letters* 42:6771–6779.
- 725 Rouse, W., R. H. Haas, W. Deering, and J. A. Schell. 1973. Monitoring the vernal advancement and  
726 retrogradation (green wave effect) of natural vegetation. Type II Report, Goddard Space Flight Center,  
727 Greenbelt, MD, USA.
- 728 Roussel, J.-R. 2019. lidRplugins: Extra functions and algorithms for lidR package.
- 729 Roussel, J.-R., D. Auty, F. De Boissieu, and A. S. Meador. 2019. lidR: Airborne LiDAR data manipulation  
730 and visualization for forestry applications.
- 731 Safford, H. D., and J. T. Stevens. 2017. Natural range of variation for yellow pine and mixed-conifer forests  
732 in the Sierra Nevada, Southern Cascades, and Modoc and Inyo National Forests, California, USA. Page 241.
- 733 dos Santos, A. A., J. Marcato Junior, M. S. Araújo, D. R. Di Martini, E. C. Tetila, H. L. Siqueira, C. Aoki, A.  
734 Eltner, E. T. Matsubara, H. Pistori, R. Q. Feitosa, V. Liesenberg, and W. N. Gonçalves. 2019. Assessment of

- 735 CNN-Based Methods for Individual Tree Detection on Images Captured by RGB Cameras Attached to UAVs.  
736 Sensors (Basel, Switzerland) 19.
- 737 Seidl, R., J. Müller, T. Hothorn, C. Bässler, M. Heurich, and M. Kautz. 2016. Small beetle, large-scale  
738 drivers: How regional and landscape factors affect outbreaks of the European spruce bark beetle. The Journal  
739 of applied ecology 53:530–540.
- 740 Seybold, S. J., B. J. Bentz, C. J. Fettig, J. E. Lundquist, R. A. Progar, and N. E. Gillette. 2018. Management  
741 of western North American bark beetles with semiochemicals. Annual Review of Entomology 63:407–432.
- 742 Shepherd, W. P., D. P. W. Huber, S. J. Seybold, and C. J. Fettig. 2007. Antennal responses of the western  
743 pine beetle, *Dendroctonus brevicomis* (Coleoptera: Curculionidae), to stem volatiles of its primary host,  
744 *Pinus ponderosa*, and nine sympatric nonhost angiosperms and conifers. Chemoecology 17:209–221.
- 745 Shiklomanov, A. N., B. A. Bradley, K. M. Dahlin, A. M. Fox, C. M. Gough, F. M. Hoffman, E. M. Middleton,  
746 S. P. Serbin, L. Smallman, and W. K. Smith. 2019. Enhancing global change experiments through integration  
747 of remote-sensing techniques. Frontiers in Ecology and the Environment 0.
- 748 Shin, P., T. Sankey, M. Moore, and A. Thode. 2018. Evaluating unmanned aerial vehicle images for estimating  
749 forest canopy fuels in a ponderosa pine stand. Remote Sensing 10:1266.
- 750 Stephenson, N. 1998. Actual evapotranspiration and deficit: Biologically meaningful correlates of vegetation  
751 distribution across spatial scales. Journal of Biogeography 25:855–870.
- 752 Stephenson, N. L., A. J. Das, N. J. Amperee, and B. M. Bulaon. 2019. Which trees die during drought?  
753 The key role of insect host-tree selection. Journal of Ecology:75.
- 754 Stovall, A. E. L., H. Shugart, and X. Yang. 2019. Tree height explains mortality risk during an intense  
755 drought. Nature Communications 10:1–6.
- 756 Thistle, H. W., H. Peterson, G. Allwine, B. Lamb, T. Strand, E. H. Holsten, and P. J. Shea. 2004. Surrogate  
757 pheromone plumes in three forest trunk spaces: Composite statistics and case studies. Forest Science 50.
- 758 USDAFS. 2019, February 11. Press Release: Survey finds 18 million trees died in California in 2018.  
759 [https://www.fs.usda.gov/Internet/FSE\\_DOCUMENTS/FSEPRD609321.pdf](https://www.fs.usda.gov/Internet/FSE_DOCUMENTS/FSEPRD609321.pdf).
- 760 Vega, C., A. Hamrouni, S. El Mokhtari, J. Morel, J. Bock, J. P. Renaud, M. Bouvier, and S. Durrieu. 2014.  
761 PTrees: A point-based approach to forest tree extraction from LiDAR data. International Journal of Applied  
762 Earth Observation and Geoinformation 33:98–108.
- 763 Weinstein, B. G., S. Marconi, S. Bohlman, A. Zare, and E. White. 2019. Individual Tree-Crown Detection in

- 764 RGB Imagery Using Semi-Supervised Deep Learning Neural Networks. *Remote Sensing* 11:1309.
- 765 Wyngaard, J., L. Barbieri, A. Thomer, J. Adams, D. Sullivan, C. Crosby, C. Parr, J. Klump, S. Raj Shrestha,  
766 and T. Bell. 2019. Emergent challenges for science sUAS data management: Fairness through community  
767 engagement and best practices development. *Remote Sensing* 11:1797.
- 768 Young, D. J. N., J. T. Stevens, J. M. Earles, J. Moore, A. Ellis, A. L. Jirka, and A. M. Latimer. 2017.  
769 Long-term climate and competition explain forest mortality patterns under extreme drought. *Ecology Letters*  
770 20:78–86.
- 771 Zhang, W., J. Qi, P. Wan, H. Wang, D. Xie, X. Wang, and G. Yan. 2016. An easy-to-use airborne LiDAR  
772 data filtering method based on cloth simulation. *Remote Sensing* 8:501.